Macroscopic quantum entanglement and 'super-rigidity' of protons in the $KHCO_3$ crystal from 30 to 300 K

2006 J. Phys.: Condens. Matter 18 3229

(http://iopscience.iop.org/0953-8984/18/12/006)

INSTITUTE OF PHYSICS PUBLISHING JOURNAL OF PHYSICS: CONDENSED MATTER

J. Phys.: Condens. Matter **18** (2006) 3229–3249 doi:10.1088/0953-8984/18/12/006

Macroscopic quantum entanglement and 'super-rigidity' of protons in the $KHCO_3$ crystal from 30 to 300 K

François Fillaux[1,4], **Alain Cousson**[2] **and Matthias J Gutmann**[3]

[1] LADIR-CNRS, UMR 7075, Université P et M Curie, 2 rue Henry Dunant, 94320 Thiais, France
[2] Laboratoire Léon Brillouin (CEA-CNRS), CE Saclay, 91191 Gif-sur-Yvette, cedex, France
[3] ISIS Facility, Rutherford Appleton Laboratory, Chilton, Didcot, OX11 0QX, UK

E-mail: fillaux@glvt-cnrs.fr

Received 1 November 2005, in final form 30 January 2006
Published 6 March 2006
Online at stacks.iop.org/JPhysCM/18/3229

Abstract

We utilize neutron diffraction techniques to study dynamical correlation of protons in the ionic crystal of potassium hydrogen carbonate ($KHCO_3$). Protons are found in small planar centrosymmetric dimer entities, $(HCO_3^-)_2$, linked by moderately strong hydrogen bonds and well separated by the stacking of potassium atoms. There is no disordering at low temperature and rods of diffuse scattering in (a^*, c^*) planes, not observed for $KDCO_3$, reveal macroscopic entanglement. We propose a theoretical framework for the degenerate lattice of indistinguishable protons, treated as fermions. Entangled centrosymmetric pairs are superpositions of singlet-like and triplet-like pseudoproton states and the sublattice is a superposition of nonlocal macroscopic single-pseudoproton states, adiabatically separated from the lattice of heavy atoms. The sublattice has no internal dynamics (super-rigidity) and is decoherence free. The energy-free quantum entanglement is a consequence of the crystal structure, irrespective of proton–proton interaction. The differential cross-section calculated for the super-rigid lattice accounts for the observed rods of intensity. Between 150 and 300 K, protons are progressively transferred to secondary sites at ≈0.6 Å from the main position, via tunnelling along hydrogen bonds. Quantum entanglement, still observed at 300 K, indicates that proton transfer is a thermally activated coherent superposition of macroscopic tunnelling states. This work adds a crystalline solid to the list of systems with 'super' properties.

(Some figures in this article are in colour only in the electronic version)

[4] Author to whom any correspondence should be addressed (http://www.ladir.cnrs.fr/pagefillaux_eng.htm).

1. Introduction

The linear formalism of quantum mechanics extrapolated from the level of electrons and atoms to that of everyday life can lead to conclusions in conflict with our commonsense intuition, such as Schrödinger's cat in a superposition of 'alive–dead' states, or the Einstein–Podolsky–Rosen (EPR) paradox [1] challenging the classical concept of locality. Such conflicts can lead to a dichotomy of interpretation in that, while at the microscopic level a quantum superposition indicates a lack of definiteness of outcome, at the macroscopic level a similar superposition can be interpreted as simply a measure of the probability of one outcome or the other, one of which is definitely realized for each measurement of the ensemble [2–7].

The dichotomy of interpretation is legitimated by decoherence [8]. In complex systems, an initially entangled subsystem loses its ability to exhibit quantum interference by getting entangled with many degrees of freedom via interaction with the environment. In the condensed matter this process normally occurs on a very short timescale ($\lesssim 10^{-15}$ s) [9], but it is unknown whether there is an upper limit on the timescale, the size and the complexity of systems displaying entanglement.

Upon the assumption that decoherence is the only cause preventing the persistence of superposition states, macroscopic quantum behaviour is possible for systems decoupled from the environment [10]. Recent studies of the potassium hydrogen carbonate crystal ($KHCO_3$) have revealed a class of nonferro/nonantiferroelectric and nonmagnetic ionic solids for which macroscopic quantum behaviour arises naturally for entangled pairs of protons in centrosymmetric dimer entities $(HCO_3^-)_2$ linked by moderately strong hydrogen bonds (figure 1) [11, 12]. Decoherence is cancelled by the dynamical separation of protons from the rest of the lattice [13]. Neutron diffraction reveals, in addition to Bragg's peaks, rods of diffuse scattering, suggesting the existence of macroscopic states for a number of atoms on the scale of Avogadro's constant.

So far, experiments on $KHCO_3$ were carried out at 14 K, a temperature at which protons are ordered. The motivation of the present work is to test whether quantum coherence survives at higher temperatures in the presence of proton transfer along the hydrogen bonds, commonly thought of as a stochastic disordering process [14–16]. In this paper, we report evidence that quantum coherence survives at room temperature, quite at variance with any expectation. This sheds light onto proton dynamics in connection with some fundamental points of quantum mechanics applied to macroscopic systems at elevated temperatures.

The organization of this paper is the following. In section 2, crystal structures determined at various temperatures evidence the spatial coherence of proton transfer. Simultaneously, the rods of diffuse scattering, a fingerprint of quantum coherence, are largely temperature independent. The theoretical framework for quantum entanglement of protons is presented in section 3. We define pseudoproton states for entangled centrosymmetric pairs and macroscopic single-particle states for the sublattice of protons. We show that the sublattice has no internal dynamics: it is 'super-rigid'. We calculate the differential cross-section for comparison with experiments. In section 4, we introduce the quantum superposition of macroscopic tunnelling states and we emphasize the role of disentanglement in proton transfer dynamics. We conclude that the upper limit, if any, for $KHCO_3$ to display quantum entanglement is beyond Avogadro's constant and room temperature.

2. Neutron diffraction experiments

Twining-free single crystals of $KHCO_3$ were obtained by slow recrystallization from aqueous solutions.

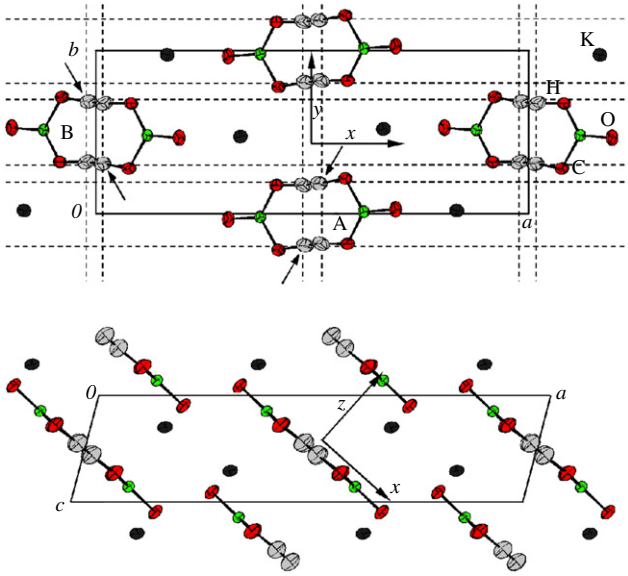

Figure 1. Schematic view of the crystalline structure of $KHCO_3$ at 300 K. Apart from proton positions and thermal ellipsoids, the structure is identical to that at 14 K [12]. The arrows point to the sites exclusively occupied by protons at low temperature. Top: projection onto the plane normal to (c). The dotted lines joining protons are guides for the eyes to emphasize the structure of the proton sublattice (see the text). Bottom: projection onto the plane normal to (b).

2.1. Crystal structure

Measurements were conducted with the Stoe four-circle diffractometer 5C2 at the Orphée reactor (Laboratoire Léon Brillouin) [17]. Approximately cubic samples ($3 \times 3 \times 3$ mm^3) were cut from large crystals and tested at room temperature. An oriented crystal was loaded into an aluminium container that was mounted in a cryostat. The temperature was controlled to ± 1 K.

The structures at 150, 200 and 300 K (table 1) are similar to those previously reported [18, 19, 12]. The crystal is monoclinic, space group $P2_1/a$ (C_{2h}^5), with four $KHCO_3$ entities per unit cell (figure 1 and tables 2–4). Protons are found in small planar centrosymmetric dimer entities $(HCO_3)_2^-$ well separated by the stacking of potassium atoms. All dimers lie practically in the $(30\bar{1})$ planes and hydrogen bonds are also virtually parallel to the same direction. The increase of the unit cell dimensions with temperature is marginal. Needless to say, the crystal is nonferro/nonantiferroelectric and nonmagnetic at any temperature.

At 150 K protons are still localized at a single site (configuration **I**, see arrows in figure 1). All protons are crystallographically equivalent and indistinguishable. At higher temperatures, the probability density is distributed among two sites located at $\approx \pm 0.3$ Å off-centre of the hydrogen bond (figure 2 and tables 2 and 3). The centre of symmetry is preserved and secondary proton sites (configuration **II**) are also crystallographically equivalent and indistinguishable. **I** and **II** are related through translation $(a/2, b/2, 0)$.

Proton transfer does not change Bragg's peak positions and there is no evidence for additional peaks. Only intensities are affected. Consequently, the crystal lattice and the geometry of the CO_3^{2-} entities remain unchanged by proton transfer. Configurations **I** and **II** are distinct in direct space and isomorphous in reciprocal space.

Table 1. Neutron single crystal diffraction data and structure refinement for potassium hydrogen carbonate at various temperatures. $\lambda = 0.8305$ Å, space group $P2_1/a$. The variance for the last digit is given in parentheses.

Crystal data	14 K [12]	150 K	200 K	300 K
a (Å)	15.06(2)	15.098(8)	15.112(8)	15.18(1)
b (Å)	5.570(15)	5.597(4)	5.601(4)	5.620(4)
c (Å)	3.650(8)	3.665(4)	3.671(4)	3.710(4)
α (deg)	90	90	90	90
β (deg)	103.97(15)	104.14(5)	104.32(5)	104.67(5)
γ (deg)	90	90	90	90
Volume	297.1	300.3	301.1	306.2
Reflections measured	1857	2137	2075	1731
Independent reflections	979	1881	1332	1475
Reflections used	904	1073	1044	1068
σ(I) limit	3.00	3.00	3.00	3.00
Refinement on F				
R-factor	0.026	0.037	0.032	0.035
Weighted R-factor	0.020	0.029	0.032	0.034
Number of parameters	56	56	56	56
Goodness of fit	1.070	1.028	0.84	1.025
Extinction	4040(80)	32.0(10)	76.3(21)	3260(100)

Table 2. Atomic positions, isotropic temperature factors and site occupancies for $KHCO_3$ at 150 K (first lines), 200 K (second lines), and 300 K (third lines). The variance for the last digit is given in parentheses.

Atom	x/a	y/b	z/c	U(iso) (Å^2)	Occupancy
K(1)	0.165 79(4)	0.034 51(12)	0.294 90(17)	0.0078	1.000
	0.165 68(6)	0.033 10(16)	0.295 0(2)	0.0127	1.000
	0.165 34(6)	0.022 98(16)	0.295 2(2)	0.0213	1.000
C(2)	0.119 63(2)	0.524 87(6)	−0.145 20(9)	0.0062	1.000
	0.119 59(3)	0.523 70(8)	−0.145 12(12)	0.0104	1.0000
	0.119 57(3)	0.516 36(8)	−0.144 40(11)	0.0164	1.000
O(1)	0.193 44(3)	0.545 97(8)	0.094 79(12)	0.0105	1.000
	0.193 43(4)	0.544 04(11)	0.094 68(17)	0.0161	1.000
	0.193 44(4)	0.530 65(12)	0.094 57(18)	0.0259	1.000
O(2)	0.083 02(3)	0.330 14(8)	−0.274 69(12)	0.0096	1.000
	0.082 94(4)	0.329 0(1)	−0.274 43(16)	0.0148	1.000
	0.082 37(4)	0.320 6(1)	−0.273 54(18)	0.0238	1.000
O(3)	0.076 23(3)	0.729 84(8)	−0.275 20(13)	0.0101	1.000
	0.076 32(4)	0.728 0(1)	−0.275 27(17)	0.0152	1.000
	0.077 45(4)	0.718 6(1)	−0.274 25(19)	0.0243	1.000
H(1)	0.015 11(6)	0.693 61(16)	−0.452 4(3)	0.0197	1.000
	0.015 23(9)	0.692 9(2)	−0.452 1(4)	0.0237	0.959(4)
	0.016 31(12)	0.690 5(2)	−0.449 1(5)	0.0330	0.823(4)
H(2)	—	—	—	—	—
	0.020(2)	−0.170(5)	0.551(9)	0.0237	0.042(4)
	−0.0207(6)	0.6797(11)	−0.563(2)	0.0338	0.177(4)

The sum of probability densities at the proton sites is unity and temperature independent, to within experimental errors (table 2). This is at odds with a random distribution of tautomers [14–16] that should destroy long range correlations at elevated temperatures. If

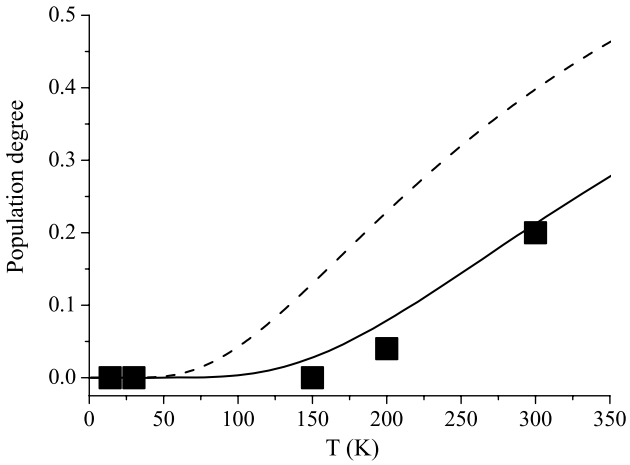

Figure 2. Population degrees of the secondary proton sites as a function of temperature. ■: experiments. Solid line: equation (17) for entangled states. Dashed line: equation (19) for disentangled states.

Table 3. Interatomic distances in Å units and angles in degrees in $KHCO_3$ at 150 K (first lines), 200 K (second lines) and 300 K (third lines). The variance for the last digit is given in parentheses.

C(1)–O(1)	1.245(2)	O(1)–C(1)–O(2)	125.60(5)
	1.2439(13)		125.38(8)
	1.2434(6)		123.92(5)
C(1)–O(2)	1.2611(13)	O(1)–C(1)–O(3)	116.26(5)
	1.2614(12)		116.45(9)
	1.2734(7)		117.78(5)
C(1)–O(3)	1.3490(14)	O(2)–C(1)–O(3)	118.14(11)
	1.3458(13)		118.16(8)
	1.3331(7)		118.30(4)
O(3)–H(1)	1.011(2)	C(1)–O(3)–H(1)	110.16(15)
	1.0080(17)		110.47(11)
	1.001(2)		112.38(9)
O(2)–H(2)	—	C(1)–O(2)–H(2)	—
	1.00(3)		119.6(16)
	0.978(9)		119.9(4)
H(1)–H(2)	—	O(3)–H(1)–H(2)	—
	0.58(3)		178.0(31)
	0.615(8)		175.7(7)
H(1)–H(2)	—	O(2)–H(2)–H(1)	—
	2.224(6)		167.2(44)
	2.208(8)		172.2(11)

it were the case, a significant amount of the coherent scattering should collapse into off-Bragg peak diffuse scattering [20], and a decrease of the total density should be observed. Contrariwise, neutron diffraction reveals that proton transfer does not destroy the spatial coherence. If this is confirmed, the crystal should be a superposition of configurations **I** and **II** instead of a distribution of uncorrelated tautomers.

As a general trend, the U_{ii} in table 4 are multiplied by factors of ≈2–3 between 150 and 300 K and ≈4–6 between 14 K [12] and 300 K. These values reflect the thermal expansion

Table 4. Thermal parameters in Å^2 units for $KHCO_3$ at 150 K (first lines), 200 K (second lines) and 300 K (third lines). The variance for the last digit is given in parentheses. These parameters account for the contribution of each atom to Bragg's peak intensities through the thermal factor $T^{at} = \exp[-2\pi^2(U_{11}^{at}h^2a^{*2} + U_{22}^{at}k^2b^{*2} + U_{33}^{at}l^2c^{*2} + 2U_{12}^{at}ha^*kb^* + 2U_{23}^{at}kb^*lc^* + U_{31}^{at}lc^*ha^*)]$, where a^*, b^*, and c^* are the reciprocal lattice parameters and h, k, and l the indices in reciprocal space.

Atom	U_{11}	U_{22}	U_{33}	U_{23}	U_{13}	U_{12}
K(1)	0.009 0(2)	0.007 0(2)	0.006 6(2)	0.000 22(17)	0.000 53(17)	0.000 36(17)
	0.014 6(3)	0.012 7(3)	0.010 1(3)	0.000 2(2)	0.001 7(2)	0.000 5(2)
	0.024 0(3)	0.022 2(3)	0.015 9(3)	−0.000 4(3)	0.001 7(2)	0.000 9(3)
C(1)	0.005 68(13)	0.006 00(15)	0.006 41(14)	−0.000 3(1)	0.000 44(9)	−0.000 03(9)
	0.009 60(18)	0.011 10(19)	0.010 16(18)	−0.000 38(13)	0.001 64(13)	−0.000 11(12)
	0.015 04(17)	0.018 18(19)	0.014 68(18)	−0.000 04(13)	0.001 62(12)	−0.000 27(13)
O(1)	0.007 23(16)	0.012 03(18)	0.010 26(17)	−0.000 75(13)	−0.001 95(12)	−0.000 02(12)
	0.011 5(2)	0.019 0(3)	0.015 3(2)	−0.001 18(18)	−0.001 34(17)	−0.000 13(16)
	0.017 7(2)	0.031 6(3)	0.023 2(2)	−0.001 5(2)	−0.004 23(17)	0.000 06(19)
O(2)	0.009 63(16)	0.005 42(18)	0.011 54(18)	−0.000 24(12)	−0.001 93(12)	0.000 13(11)
	0.014 6(2)	0.010 6(2)	0.016 4(2)	−0.000 57(16)	−0.001 55(18)	0.000 39(16)
	0.022 6(2)	0.017 9(2)	0.025 5(3)	−0.000 87(18)	−0.003 68(19)	0.000 96(17)
O(3)	0.009 40(16)	0.005 89(18)	0.0127 0(19)	−0.000 25(12)	−0.001 75(12)	−0.000 04(11)
	0.014 2(2)	0.010 4(2)	0.018 3(3)	−0.000 06(16)	−0.001 15(18)	−0.000 26(15)
	0.023 1(2)	0.017 6(2)	0.027 2(3)	0.000 72(18)	−0.003 0(2)	−0.000 60(17)
H(1)	0.017 3(3)	0.016 2(3)	0.022 5(4)	−0.000 2(3)	−0.001 1(3)	−0.000 2(2)
	0.021 1(2)	0.019 5(2)	0.027 0(2)	−0.000 4(2)	−0.000 7(2)	−0.000 1(2)
	0.034 9(2)	0.023 6(2)	0.036 9(2)	−0.002 4(2)	0.002 3(2)	−0.002 1(2)
H(2)	—	—	—	—	—	—
	0.021 1(2)	0.019 5(2)	0.027 0(2)	0.000 4(2)	0.000 7(2)	0.000 1(2)
	0.034 7(2)	0.023 7(2)	0.036 7(2)	−0.006 8(2)	−0.002 3(2)	−0.005 9(2)

of the mean square amplitudes for atom displacements. Off-diagonal terms U_{ij} are always marginal and the U_{ii} are virtually parallel to the principal axes of the thermal ellipsoids.

There is a nonferroic phase transition at $T_c = 318$ K [21, 22]. Above T_c the symmetry is $C2/m$ and the unit cell dimensions are virtually unchanged but protons are equally distributed over the two sites. Further experimental studies of this phase are in progress.

2.2. Quantum coherence

Compared to the four-circle diffractometer, the advantage of the SXD instrument at the ISIS pulsed neutron source [23] is twofold. Firstly, with the high flux of epithermal neutrons delivered by the spallation source, one can probe a much larger domain of reciprocal space than at a reactor source. Secondly, with the time-of-flight technique, the whole accessible range of reciprocal space is measured for each neutron pulse. This is convenient for seeking signals in addition to Bragg intensities.

We have measured two as-grown crystals. First, a crystal platelet $\approx 5 \times 3 \times 1$ mm^3 with the main face $(30\bar{1})$ was loaded into a closed-cycle refrigerator. Measurements were carried out at 30, 200 and 300 K. Second, a much bigger crystal $\approx 15 \times 10 \times 3$ mm^3 was loaded in a vacuum tank and then measured at 300 K. There is no visible effect related to the crystal size, apart from a substantial gain in intensity and signal-to-noise ratio. Multiple scattering events can therefore be safely neglected.

By definition, $\mathbf{Q} = \mathbf{k}_0 - \mathbf{k}_f$ is the momentum transfer vector, $\mathbf{k}_0$ and $\mathbf{k}_f$ are the incident and scattered wavevectors, respectively, with $|\mathbf{k}_0| = 2\pi/\lambda_0$ and $|\mathbf{k}_f| = 2\pi/\lambda_f$. The nods of

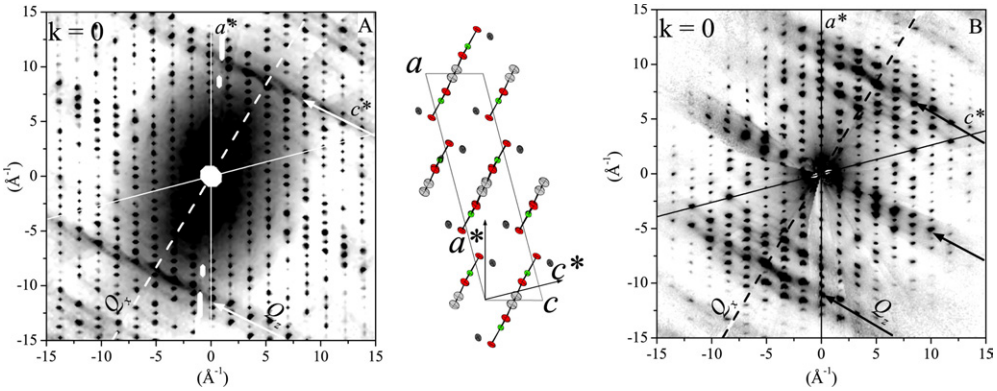

Figure 3. Diffraction patterns of $KHCO_3$ at 30 K (A) and 300 K (B) in the (a^*, c^*) plane at $k = 0$. The arrows point to the ridges of intensity along Q_z at 0 and $\approx\pm 10$ Å^{-1} from the origin along Q_x. The inset visualizes the correspondence between the direct and reciprocal lattices.

the reciprocal lattice are at $\mathbf{Q} = \mathrm{h}\mathbf{a}^* + \mathrm{k}\mathbf{b}^* + \mathrm{l}\mathbf{c}^*$, with $|\mathbf{a}^*| = 2\pi/a$, etc; Q_x, Q_y, and Q_z are projections onto the x, y, and z axes parallel to the stretching (ν OH in the 2000–3500 cm^{-1} range), in-plane bending (δ OH $\approx$ 1400 cm^{-1}), and out-of-plane bending (γ OH $\approx$ 1000 cm^{-1}) modes, respectively (figure 1) [11, 24]. Maps of intensity in (a^*, c^*) reciprocal planes, for cuts perpendicular to (b^*) at different k values ($k = Q_y/b^*$, with $b^* \approx 1.1118$ Å^{-1} at 300 K) are presented in figures 3–6.

The diffraction pattern at 30 K (figure 3(A)) is practically identical to that previously measured at 15 K for a different crystal with an older version of the instrument [12]. In addition to Bragg's peaks and to the anisotropic continuum of intensity centred at $\mathbf{Q} = 0$ due to incoherent scattering, ridges of intensity along Q_z are clearly visible.

At 300 K, both Bragg's peaks and incoherent scattering are largely depressed at large $|\mathbf{Q}|$-values. By contrast, the ridges of intensity are better visible (figure 4(B)). There are clearly three ridges parallel to Q_z. With hindsight, the ridge going through the centre is also barely visible at low temperature [12].

The weak temperature effect to the ridges is emphasized by cuts of the diffraction patterns parallel to (a^*). For example, the cuts at $-(4.5 \pm 0.2)$ Å^{-1} from (a^*) presented in figure 4 are free of Bragg's peaks. The sharp peaks correspond to the intercept of the cutting line with the ridge. The intensity at maximum is similar to that for incoherent scattering at $\mathbf{Q} = 0$. The peaks are superimposed on the broad continuum arising from incoherent scattering. As the temperature is increased, the intensity of the ridge remains approximately constant, while that of the incoherent background decreases. This suggests decoupling of the ridge intensity from the Debye–Waller factor.

The peak position in figure 4 shifts smoothly from $-(9.25 \pm 0.2)$ Å^{-1} at 15 K to $-(9.0 \pm 0.2)$ Å^{-1} at 300 K. This marginal effect shows that the rods, like Bragg's peaks, are largely insensitive to proton transfer. In fact, configurations **I** and **II** gives the same systems of rods. On the other hand, the increasing width from 0.44 to 1.0 Å^{-1} is consistent with a decreasing of the coherence length.

Cuts of the diffraction pattern perpendicular to (b^*) reveal a rather complex pattern of ridges in (a^*, c^*) planes depending on k (figure 5). At $k = 1$, the lines are barely visible [12]. At $k = 2$ or 3, we observe a new pattern composed of ridges at $Q_x \approx \pm(5 \pm 0.2)$ and $\pm(15 \pm 0.2)$ Å^{-1}, still along Q_z. There is no visible ridge at $k = 4$. Then, from $k = 5$ to 9,

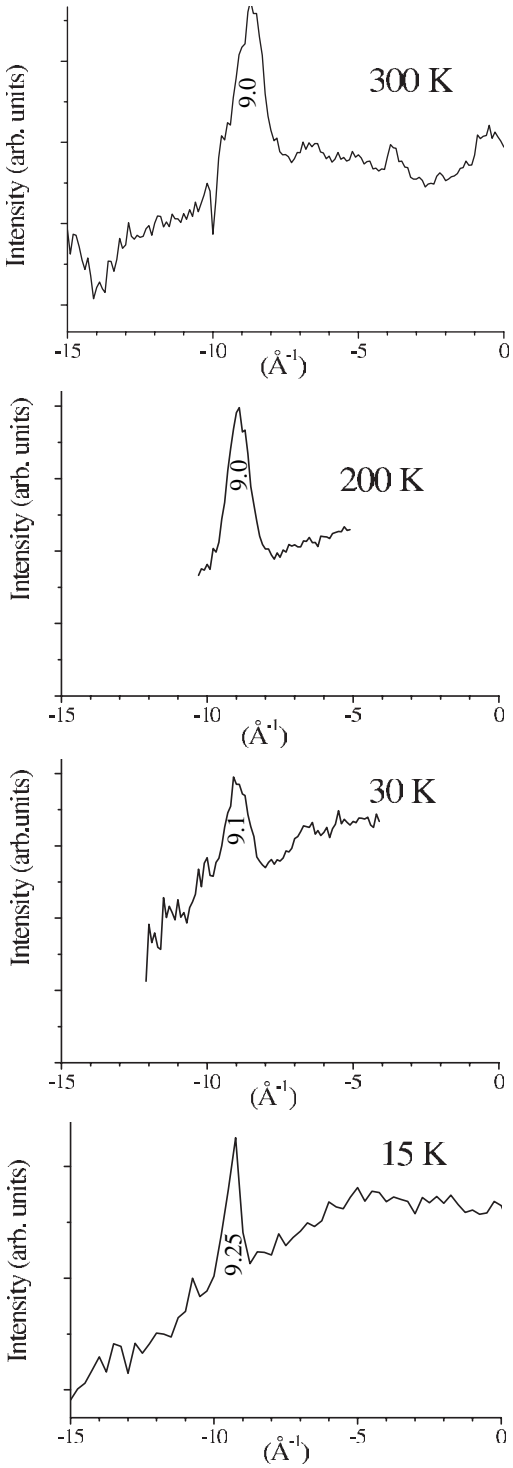

Figure 4. Cuts of the diffraction pattern of $KHCO_3$ in the (a^*, c^*) plane parallel to (a^*) and at (-4.5 ± 0.2) Å^{-1} from this axis. For the sake of comparison, the cut at 15 K is reported from [12].

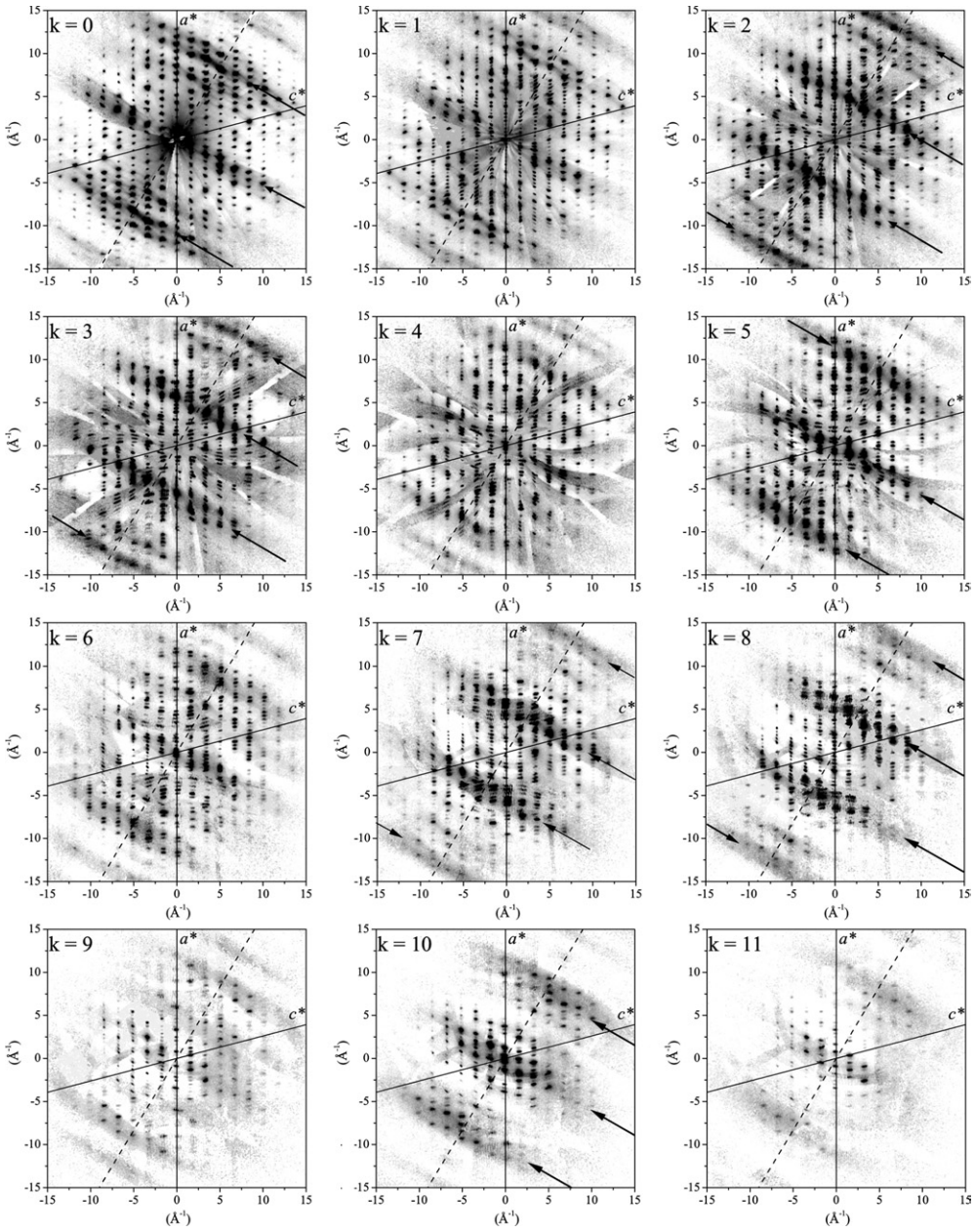

Figure 5. Cuts of the diffraction pattern of $KHCO_3$ at 300 K in various (a^*, c^*) planes. The arrows emphasize ridges of intensity parallel to Q_z and perpendicular to the dimer plane (dashed lines along Q_x).

we observe the same sequence of patterns as for $k = 0$ to 4. The ridges along Q_x and Q_y are clearly correlated.

2.3. Experimental conclusions

In principle, one can envisage several phenomena to interpreting the ridges.

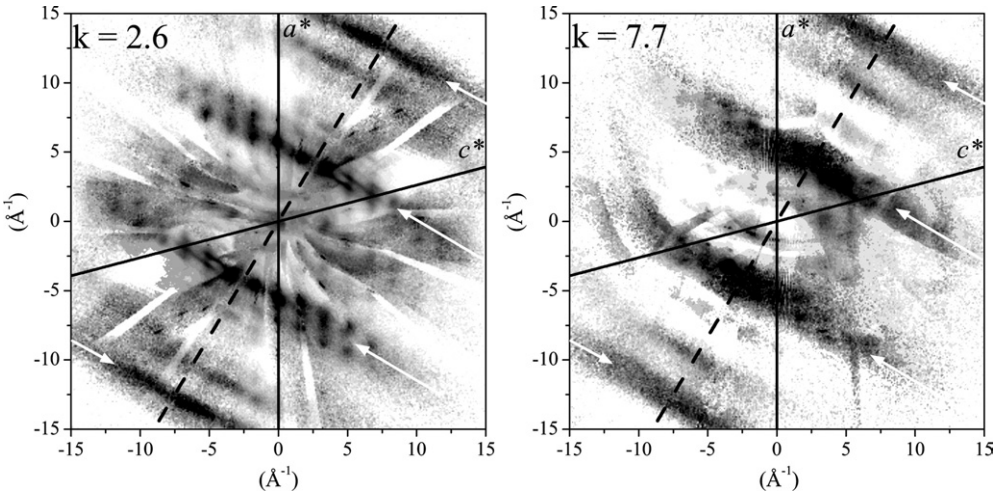

Figure 6. Diffuse scattering of $KHCO_3$ at 300 K in between (a^*, c^*) reciprocal planes. The arrows emphasize ridges of intensity parallel to Q_z and perpendicular to the dimer plane (dashed lines along Q_x).

- Multiple scattering can be discarded since there is no significant change of the ridges with the sample size. Moreover, it is unlikely that multiple scattering events, essentially incoherent, could give such a wealth of ridges as shown in figure 5.
- The ridges are quite different from the streaks of diffuse scattering observed in systems with anisotropic disordering [20]. For hydrogenous materials, observation with neutrons of diffuse scattering due to proton disordering is normally difficult because of the large incoherent scattering contribution. The contrast is greatly improved for deuterated samples, thanks to the more favourable ratio for coherent and incoherent cross sections. Clearly, the ridges in question for $KHCO_3$ are different in nature. They are observed at low temperature, although there is no disordering, and they are no longer observed for $KDCO_3$ [12], in spite of the increased coherent cross-section. Moreover, at elevated temperatures, possible disordering due to proton transfer along the hydrogen bonds should give rise to diffuse scattering along Q_x that is not observed. Contrariwise, there is no evidence for position disordering along z that could contribute to the diffuse scattering observed along Q_z. (Any further comparison with streaks arising from electric or magnetic disordering is pointless.)
- Incoherent scattering can be also rejected since the ridges at $Q_x \approx \pm 10$ Å^{-1} are well separated from the incoherent scattering continuum and there is no visible counterpart in INS [11, 25].
- Finally, the ridges have all the characteristics anticipated for coherent elastic scattering by the entangled sublattice of protons [12]:
  - * They are clearly separated from Bragg peaks.
  - * Orientations correspond to momentum transfer Q_z perpendicular to dimer planes.
  - * Positions at $Q_x = \pm(10.25 \pm 0.25)$ Å^{-1} are in accordance with the spacing of double lines of protons (about 0.6 Å).
  - * The width along (b^*) is similar to that of Bragg peaks (rod-like shape).

In the next section, we propose a theoretical model. Before this, for the sake of clarity, the salient experimental conclusions (**EC**) can be featured as follows.

EC1: For each of the distinct configurations **I** and **II**, proton sites are indistinguishable.
EC2: Proton transfer does not destroy the spatial coherence.
EC3: Ridges of intensity are fingerprints for quantum correlations.
EC4: Quantum correlations are decoupled from the Debye–Waller factor.

3. Quantum entanglement in a lattice of hydrogen bonded centrosymmetric dimers at $T = 0$

Different theoretical frameworks have been proposed for the rods of intensity at low temperature [13, 11, 12, 26–30]. All of them take into consideration the quantum origin of the rods. They suppose protons to behave as fermions and, therefore, to undergo quantum entanglement. However, quantum correlations, either for isolated pairs [26, 29, 30], or for collective dynamics of pairs thought of as composed bosons [12], analogous to Cooper pairs in superconductivity or ^{3}He pairs in superfluidity, are not in accordance with the persistence of the rods at room temperature, as reported in the previous section. According to the existing theories, the rod intensity should be dramatically depressed at elevated temperatures by the Debye–Waller factor. These theories must be amended and, for this purpose, we start with the following premises.

(i) For each configuration of the sublattice, proton sites are indistinguishable.
(ii) Proton dynamics are adiabatically separable from heavy atoms.
(iii) Protons are fermions.
(iv) For each configuration, protons are degenerate. The overlap of the vibrational wavefunctions is rigorously negligible and so is the exchange energy [27]. Spin–spin interaction is also negligible.

These premises are firmly based on experiments. (i) is established by diffraction (**EC1**). (ii) is a relevant approximation for hydrogen bonds [31]. (iii) accounts for quantum correlations (**EC3**). This fermion behaviour arises from the decoupling of protons from the chemical environment due to hydrogen bonding.

Finally, (iv) is a consequence of the distances (≈2.22 Å) between nearest-neighbour protons. This is at variance with the proposal by Keen and Lovesey [26] and Lovesey [29] that quantum entanglement arises from the overlap integral S of the nuclear wavefunctions. This assumption is incorrect. A straightforward estimate gives $S \sim 10^{-35}$ [27]. Clearly, $S \equiv 0$ for all practical purposes. Note that (iv) is also at variance with the statement by Sugimoto *et al* [30], after Cowley [32], that quantum entanglement necessarily splits the ground state and that this splitting should be spectroscopically resolved in order to observe quantum interferences. Elastic neutron scattering experiments on $KHCO_3$ is an unquestionable counter example [11]. Furthermore, to speculate an exchange energy on the order of 1 meV [30] is unrealistic.

3.1. The crystal of protons

Consider an ideal crystal composed of very large numbers N_a, N_b, N_c ($\mathcal{N} = N_a N_b N_c$), of unit cells labelled j, k, l, along the crystal axes (a), (b), (c), respectively. For each unit cell there are two dimer entities (labelled A and B in figure 1) related through the (a, c) glide plane. These dimers are indexed as jkl and $j'kl$, respectively, with, not forgetting they are indistinguishable, $j = j'$. Within the framework of the Born–Oppenheimer approximation, we start with the vibrational Hamiltonian for configuration **I** at $T = 0$:

$$\mathcal{H} = \mathcal{H}_{\mathrm{H}} + \mathcal{H}_{\mathrm{at}} + \mathcal{C}_{\mathrm{Hat}} \tag{1}$$

where $\mathcal{H}_{\rm H}$ and $\mathcal{H}_{\rm at}$ represent the sublattices of protons and heavy atoms (KCO_3^-), respectively, and $\mathcal{C}_{\rm Hat}$ contains coupling terms between the two subsystems. For hydrogen bonds coupling terms between OH (especially the stretching) and O···O degrees of freedom are rather strong while other coupling terms are negligible [31, 33].

In the harmonic approximation, the normal coordinates ξ_t of $\mathcal{H}$ are linear combinations of the normal coordinates x_r and X_s for $\mathcal{H}_{\rm H}$ and $\mathcal{H}_{\rm at}$, respectively: $\xi_t = \sum_r \sum_s c_{rs} x_r X_s$. The Gaussian wavefunctions $\Psi_{t,0}(\xi_t)$ are not factorable and cannot be antisymmetrized with respect to proton permutations. The fermion nature of protons is hidden [13]. However, thanks to the light mass of protons compared to other atoms, dynamics are adiabatically separable [31] and wavefunctions depending parametrically on lattice coordinates $\{X\}$ can be properly antisymmetrized. In the harmonic approximation, the Hamiltonian for protons can be written as

$$\begin{aligned}
\mathcal{H}_0 &= \sum_{j=j'=1}^{N_a} \sum_{k=1}^{N_b} \sum_{l=1}^{N_c} \sum_{\alpha} \left\{ H_{0jkl\alpha} + H_{0j'kl\alpha} \right\}, \qquad \alpha = x, y, z; \\
H_{0jkl\alpha} &= \frac{1}{2m} \left(P_{1jkl\alpha}^2 + P_{2jkl\alpha}^2 \right) + \frac{1}{2} m \omega_{0\alpha}^2 \left\{ \left[\alpha_{1jkl} - \alpha_{0jkl} \right]^2 \right. \\
&\quad \left. + \left[\alpha_{2jkl} + \alpha_{0jkl} \right]^2 + 2\lambda_{0\alpha} \left[\alpha_{1jkl} - \alpha_{2jkl} \right]^2 \right\}; \\
j &\longleftrightarrow j' : H_{0jkl\alpha} \longleftrightarrow H_{0j'kl\alpha}.
\end{aligned} \tag{2}$$

$P_{1jkl\alpha}$ and $P_{2jkl\alpha}$ are kinetic momenta. Coordinates α_{1jkl} and α_{2jkl} are projections onto the α direction of proton positions, defined with respect to the projection of the centre of symmetry of the pair jkl. The frequency of uncoupled oscillators at equilibrium positions $\pm\alpha_{0jkl}$ is $\hbar\omega_{0\alpha}$. The coupling term, essentially due to electrostatic interaction, shifts the equilibrium positions at $\pm\alpha'_{0jkl} = \pm\alpha_{0jkl}/[1 + 4\lambda_\alpha]$. The last line in (2) means that $H_{0j'kl\alpha}$ is related to $H_{0jkl\alpha}$ by substituting j' to j. In the remainder of this paper, with any equation depending solely on j is implicitly associated the same equation depending on j'. Normal coordinates and conjugated momenta

$$\begin{aligned}
\alpha_{sjkl} &= \frac{1}{\sqrt{2}} \left(\alpha_{1jkl} - \alpha_{2jkl} \right), \qquad & P_{sjkl\alpha} &= \frac{1}{\sqrt{2}} \left(P_{1jkl\alpha} - P_{2jkl\alpha} \right), \\
\alpha_{ajkl} &= \frac{1}{\sqrt{2}} \left(\alpha_{1jkl} + \alpha_{2jkl} \right), \qquad & P_{ajkl\alpha} &= \frac{1}{\sqrt{2}} \left(P_{1jkl\alpha} + P_{2jkl\alpha} \right),
\end{aligned} \tag{3}$$

split $H_{0jkl\alpha}$ into uncoupled harmonic oscillators at frequencies $\hbar\omega_{s\alpha} = \hbar\omega_{0\alpha}\sqrt{1 + 4\lambda_\alpha}$ and $\hbar\omega_{a\alpha} = \hbar\omega_{0\alpha}$, respectively, each with an effective mass $m = 1$ amu. The Gaussian wavefunctions $\Psi_0^a(\alpha_{ajkl})$ and $\Psi_0^s(\alpha_{sjkl} - \sqrt{2}\alpha'_{0jkl})$ are nonlocal and cannot be factored into wavefunctions for each particle. Protons are fully entangled into EPR-like states [1]. Then, we define the spatial wavefunctions, either symmetrical or antisymmetrical with respect to permutation

$$\Theta_{0jkl\pm} = \frac{1}{\sqrt{2}} \left[\prod_\alpha \Psi_0^a(\alpha_{ajkl}) \Psi_0^s(\alpha_{sjkl} - \sqrt{2}\alpha'_{0jkl}) \pm \prod_\alpha \Psi_0^a(\alpha_{ajkl}) \Psi_0^s(\alpha_{sjkl} + \sqrt{2}\alpha'_{0jkl}) \right], \tag{4}$$

and the antisymmetrized state vectors including spin states [34]

$$\begin{aligned}
|0jkl+\rangle_{\rm H} &= \left| \Theta_{0jkl+} \right\rangle \otimes \sum_{s1=-1/2}^{1/2} \sum_{s2>s1}^{1/2} \mathcal{A}_{12} [|1jkl : s1\rangle \otimes |2jkl : s2\rangle]; \\
|0jkl-\rangle_{\rm H} &= |\Theta_{0jkl-}\rangle \otimes \frac{1}{\sqrt{3}} \sum_{s1=-1/2}^{1/2} \sum_{s2\geqslant s1}^{1/2} \mathcal{S}_{12} [|1jkl : s1\rangle \otimes |2jkl : s2\rangle];
\end{aligned} \tag{5}$$

where $|1jkl:s1\rangle$ and $|2jkl:s2\rangle$ ($s1, s2 = \pm 1/2$) are spin state vectors, and $\mathcal{S}_{12}$ and $\mathcal{A}_{12}$ are the symmetric and antisymmetric projectors, respectively.

Equation (3) defines 'pseudoprotons' (α_s, P_s) and (α_a, P_a) corresponding to symmetric or antisymmetric displacements of two 'half-protons', respectively. The Pauli principle imposes that (α_s, P_s) be singlet-like and (α_a, P_a) triplet-like, but, in contrast to magnetic systems, there is no spin–spin interaction and no splitting. Pseudoprotons are nonseparable in the ground state. Quantum entanglement is energy free. It is dictated by the centre of symmetry and does not depend on the actual value of λ_α in (2).

Pseudoprotons become separable in excited vibrational states at $\sum_\alpha[(n_{\alpha a}+1/2)\hbar\omega_{\alpha a}+(n_{\alpha s}+1/2)\hbar\omega_{\alpha s}]$, thanks to $u-g$ splitting. The nonlocal dynamics is preserved but the spin symmetry is no longer required. This accords with a fundamental precept of quantum mechanics stating that energy transfer automatically destroys entanglement. Consequently, vibrational spectroscopy techniques utilizing neutrons, photons, etc, cannot provide direct evidence for entanglement.

Consider now dynamics of the whole sublattice of protons. Such dynamics are usually represented as phonons obeying the Bose–Einstein statistics law. Suppose, although this is not the case, that proton pairs (5) behave as composed bosons analogous to Cooper pairs in superconductors or atom pairs in superfluid ^{3}He. Then, phonons corresponding to spatially periodic excitations of dimers should be unaffected by pair permutation and could propagate [12]. However, whereas Cooper pairs or ^{3}He pairs behave as quasi-molecular bound entities, protons in $KHCO_3$ are not such bound entities because, according to **EC1**, the elementary entity in the crystal structure is $KHCO_3$, not $(KHCO_3)_2$. Thanks to the weakness of proton–proton interaction compared to the crystal field, there is no 'bosonization' of the proton pairs. Collective dynamics must be antisymmetrized upon permutation of protons, wherever they are located in the crystal, according to (i). Such permutations applied to any wave change the sign of the phase, and superposition of these anti-phase waves yields automatically zero amplitude. Hence, phonons are forbidden. The proton sublattice has no internal dynamics and can be termed 'super-rigid'. This macroscopic quantum behaviour does not depend explicitly on interactions between protons. It is dictated exclusively by the lattice symmetry.

Pseudoproton states for the superlattice can be represented as superpositions of macroscopic single-particle states that are linear combinations of the state vectors (5):

$$|0\tau s\rangle = \frac{1}{\sqrt{\mathcal{N}}}\left|\sum_{l=1}^{N_c}\sum_{k=1}^{N_b}\sum_{j=j'=1}^{N_a}\left[|0jkl\tau\rangle + s|0j'kl\tau\rangle\right]\right\rangle. \tag{6}$$

Here, $\tau =$ '$\pm$' for singlet and triplet states, $s = \pm 1$ for A and B symmetry species, respectively. The sublattice is a superposition of a macroscopic number of degenerate and nonseparable macroscopic pseudoproton states:

$$\overline{|0\rangle} = \sqrt{\mathcal{N}}\sum_{\tau,s}|0\tau s\rangle. \tag{7}$$

Each pseudoproton is evenly distributed over all sites and each site is equally occupied by all pseudoprotons. Local coordinates are totally hidden and permutation is now meaningless. These nonlocal states avoid any conflict with the symmetrization postulate of quantum mechanics. They are not factorable, nonseparable and maximally entangled.

To the best of our knowledge, there has been no other example of a super-rigid lattice ever reported. In contrast to dense Fermi gas or liquids, this lattice has no energy band structure, according to (iv). The Fermi energy is zero and there is no gapless excitation. (In $KHCO_3$, the lowest excited proton state is at $\approx$1000 cm^{-1} $\gg kT$.) In addition, the lattice is not a supersolid analogous to ^{3}He, for which the amplitude of the zero-point vibrations is similar to inter-site

distances. $KHCO_3$ can be compared to a Mott insulator. The occupancy degree is unity at each proton site and there is no possible exchange. There is no matter wave. Macroscopic states (6) and (7) describe nonlocal dynamics of atoms tightly bound to their sites. For each substate, the wavefunctions oscillate synchronously in phase throughout the crystal.

In the adiabatic regime, macroscopic entanglement is intrinsically decoherence free. Upon irradiation by photons, neutrons, etc, transient disentanglement may single out some pseudoproton states, namely $\bigotimes_\alpha(\overline{|n_{\alpha a}\rangle} \otimes \overline{|n_{\alpha s}\rangle})$. However, re-entanglement occurs automatically after decaying to the ground state, by virtue of indistinguishability. Massive decoherence is cancelled out. Energy-free re-entanglement on the timescale of proton dynamics ($\sim 10^{-13}$–10^{-14} s) is the key mechanism keeping the sublattice at thermal equilibrium with the surroundings, despite the lack of internal dynamics. Similarly, the sublattice of protons can adapt itself to structural changes with temperature and pressure. Note that even at room temperature the thermal population of the lowest excited proton state is rather small ($\sim 10^{-2}$). Quantum entanglement in the ground state is prevailing, although the coherence length decreases.

For the deuterated analogue, $KDCO_3$, equations (4) and (5) are irrelevant. The ground state wavefunction for dimers, namely $\prod_\alpha \Psi_0^a(\alpha_{ajkl})\Psi_0^s(\alpha_{sjkl} - \sqrt{2}\alpha_{0jkl})$, is symmetrical with respect to permutation and spin correlation is not required. Dynamics are represented as nonlocal pseudodeuterons according to (3) and phonons are allowed. Needless to say, the numbers of degrees of freedom are identical for the two systems. The main consequence of entanglement is to shrink the allowed Hilbert space from $\sim 12^{\mathcal{N}}$ for bosons to $\sim 12\mathcal{N}$ for fermions. (Note that there are 12 degrees of freedom per unit cell.)

3.2. Cross-sections for neutron scattering

The differential cross-section for elastic scattering by a super-rigid lattice of protons can be written as [20, 35]

$$\frac{\mathrm{d}\sigma}{\mathrm{d}\Omega} = \left|\sum_r b_{\mathrm{H}r} \exp -\mathrm{i}\mathbf{Q}\cdot\mathbf{R}_r\right|^2 = \sum_{r,r'} \overline{b^*_{\mathrm{H}r'} b_{\mathrm{H}r}} \exp \mathrm{i}\mathbf{Q}\cdot(\mathbf{R}_r - \mathbf{R}_{r'})\,. \tag{8}$$

The time independent lattice vector at site r is $\mathbf{R}_r$. The index r includes all indices j, j', k, l, in (2). The initial and final states are identical, the Debye–Waller factor is unity and the cross-section is temperature independent. These features ideally match those of the rods. The scattering operator is b_{H} and $\overline{b^*_{\mathrm{H}r'} b_{\mathrm{H}r}}$ is averaged over nuclear spin orientations. If there were no correlation,

$$\overline{b^*_{\mathrm{H}r'} b_{\mathrm{H}r}} = |\overline{b_{\mathrm{H}}}|^2 + \delta_{r,r'}\left(\overline{|b_{\mathrm{H}}|^2} - |\overline{b_{\mathrm{H}}}|^2\right) = \frac{\sigma_{\mathrm{H}c}}{4\pi} + \delta_{r,r'}\frac{\sigma_{\mathrm{H}i}}{4\pi}. \tag{9}$$

The first term concerns Bragg diffraction. For protons $\sigma_{\mathrm{H}c} = 4\pi|\overline{b_{\mathrm{H}}}|^2 \approx 1.8$ barns (1 barn $= 10^{-24}$ cm^2). The second term holds for incoherent scattering that probes the autocorrelation function ($r = r'$). For a super-rigid lattice, this gives a single peak at $\mathbf{Q} = 0$. The cross-section $\sigma_{\mathrm{H}i} = \sigma_{\mathrm{H}} - \sigma_{\mathrm{H}c} \approx 80$ barns is quite large.

Alternatively, for fully entangled protons, $b_{\mathrm{H}r}$ and $b_{\mathrm{H}r'}$ are correlated. There is no incoherent scattering and the total cross-section is $\sigma_{\mathrm{H}} = 4\pi|b_{\mathrm{H}}|^2 \approx 81.8$ barns. The contrast $\sigma_{\mathrm{H}}/\sigma_{\mathrm{H}c} \approx 45$ is quite favourable to distinguishing macroscopic quantum correlation among Bragg's peaks, especially at large $\mathbf{Q}$ values for which incoherent scattering is depressed.

3.3. Neutron scattering

Neutron scattering can be decomposed into distinct scattering events. First, Bragg's peaks occur at nodes of the reciprocal lattice. Except for very particular orientations of **Q**, momentum transfer destroys quantum entanglement. Only the probability density is measured. Second, incoherent scattering by protons gives an anisotropic continuum of intensity, with a Gaussian-like shape centred at $\mathbf{Q} = 0$. Third, quantum coherence is probed for particular **Q**-vectors, when components Q_x, Q_y, or Q_z correspond to nodes of the reciprocal superlattice.

In practical experiments, the transversal coherence length of a neutron beam emitted by a remote source is about the beam section itself ($\approx$10 cm^2). Therefore, macroscopic quantum entanglement can be probed on the same scale.

Diffraction patterns arising from quantum entanglement can be rationalized as follows. Protons in dimer planes are aligned along directions parallel to y (dotted lines in figure 1) and quantum entanglement along this direction can be probed by elastic scattering at $Q_y = 0$. The vector state obtained by summation along y, namely

$$|0jl\tau s\rangle = \frac{1}{\sqrt{N_b}} \left| \sum_{k=1}^{N_b} \left[|0jkl\tau\rangle + s|0j'kl\tau\rangle \right] \right\rangle, \tag{10}$$

is equivalent to a double line of scatterers separated by $2x'_0$, with some similarity to double slits. Similar double lines are visible along x. Elastic neutron scattering shows interference fringes compatible with these double lines of entangled protons [11].

We show below (sections 3.3.1 and 3.3.2) that neutron diffraction by the coherent structures in two dimensions composed of double lines parallel to dimer planes gives the rods of intensity parallel to Q_z, effectively observed for particular values of Q_x and Q_y. Finally, totally coherent elastic scattering by the whole sublattice gives sharp peaks with dramatically enhanced intensities (see below section 3.3.3).

3.3.1. Quantum grating. The lines of protons parallel to y form a grating-like structure composed of two indistinguishable subsets of double lines corresponding to dimers labelled A and B, respectively (figure 1). The distance between equivalent double lines is $D_x \approx a/\cos 42^\circ \approx 20.39(2)$ Å. We consider coherent scattering as a function of Q_x, incoherent scattering along Q_z, and we set $Q_y = 0$. The differential cross-section (8) reads as

$$\frac{\mathrm{d}\sigma_2}{\mathrm{d}\Omega} = \sum_{\tau_i} \sum_{\tau_f} \sum_{k=1}^{N_b} \sum_{l=1}^{N_c} \left| \sum_{j=j'=1}^{N_a} \mathcal{F}_1(j) + \tau_f \tau_i \exp \mathrm{i}(Q_x D_x/2) \mathcal{F}_1(j') \right|^2 \exp(-2W_z); \tag{11}$$

$$\mathcal{F}_1(j) = b_{\mathrm{H}jkl} \left[\exp \mathrm{i} Q_x \left(j D_x - x'_0 \right) + \tau_f \tau_i \exp \mathrm{i} Q_x \left(j D_x + x'_0 \right) \right].$$

Here, $\exp(-2W_z)$ is the Debye–Waller factor along z. This equation diverges at $Q_x = \pm n_x \pi / x'_0 \approx \pm n_x 10$ Å^{-1}, for $\tau_i = \tau_f$ (in-phase scattering by each double lines). Then, we estimate $Q_x D_x/\pi \approx \pm n_x 68$ and $\tau_f \tau_i \exp \mathrm{i}(Q_x D_x/2) = 1$ (in-phase scattering by the subgratings). Note that the phase matching condition, namely that x'_0 be commensurable with D_x, is intrinsic to the crystal structure. The rods of intensity for $n_x = 0, \pm 1$, are visible in figure 3. Rods anticipated at larger Q_x values are beyond the measured range. Alternatively, for $Q_x = \pm(n_x + 1/2)\pi/x'_0$ and $\tau_i \neq \tau_f$, then $\tau_f \tau_i \exp \mathrm{i}(Q_x D_x/2) = -1$. Anti-phase diffraction by the two subgratings cancels out.

In figure 4, the rods observed at $Q_x = \pm(10.15 \pm 0.10)$ Å^{-1} at 30 K smoothly shift to $\pm(10.06 \pm 0.10)$ Å^{-1} at 300 K. The estimated interline spacing increases from $2x'_0 = (0.619 \pm 0.010)$ Å to (0.625 ± 0.010) Å. These distances are very close to those estimated from Bragg diffraction. The profile of intensity along the rods is identical to that of a cut

Table 5. Orders n_y, n_x and positions Q_y, Q_x of rods of intensity arising from the network of entangled orthogonal double lines of protons in two dimensions. $Q_y D_y/\pi$ is rounded to integers.

n_y	Q_y (Å^{-1})	$Q_y D_y/\pi$	$k = Q_y/b^*$	Q_x
0	0	0	0	$n_x\pi/x'_0$
1	2.86	5	2.57	$(n_x + 1/2)\pi/x'_0$
2	5.71	10	5.14	$n_x\pi/x'_0$
3	8.57	15	7.71	$(n_x + 1/2)\pi/x'_0$
4	11.42	20	10.27	$n_x\pi/x'_0$

along Q_z through the centre of the incoherent scattering intensity [12]. As the temperature is increased, there is a parallel narrowing of incoherent scattering at the centre and along the ridges. Consequently, it is almost impossible to distinguish the rod anticipated at $Q_x = 0$ from the incoherent scattering signal (see below section 3.3.3).

3.3.2. Quantum array. The differential cross-section for arrays of double lines parallel to x and y is

$$\frac{\mathrm{d}\sigma_{22}}{\mathrm{d}\Omega} = \sum_{\tau_i}\sum_{\tau_f}\sum_{l=1}^{N_c}\left|\sum_{j=j'=1}^{N_a}\mathcal{F}_2(j) + \tau_f\tau_i \exp \mathrm{i}(Q_x D_x/2 + Q_y D_y/2)\mathcal{F}_2(j')\right|^2 \exp(-2W_z);$$
$$\mathcal{F}_2(j) = \sum_{k=1}^{N_b} b_{\mathrm{H}jkl}\left\{\exp \mathrm{i}\left[Q_x\left(jD_x - x'_0\right) + Q_y\left(kD_y - y'_0\right)\right]\right. \qquad (12)$$
$$\left. + \ \tau_f\tau_i \exp \mathrm{i}\left[Q_x\left(jD_x + x'_0\right) + Q_y\left(kD_y + y'_0\right)\right]\right\}.$$

The grating-like structure along y is composed of subsets of double lines of protons corresponding to lines of dimers, either A or B, along x. The interline spacing is $2y'_0 \approx 2.209$ Å and the two subsets are symmetrical with respect to x. Divergence may occur at $Q_y = n_y\pi/y'_0 \approx n_y 2.86$ Å^{-1} since $Q_y D_y/\pi \approx n_y 5$ suggests that y'_0 is commensurable with D_y. Alternatively, there is no divergence at $Q_y = \pm(n_y + 1/2)\pi/y'_0$ since $Q_y D_y/\pi \approx (n_y + 1/2)5$ is not integer. The anticipated rods are presented in table 5. For n_y even, $Q_y D_y/\pi$ is also even, $\tau_i = \tau_f$, and ridges are anticipated at $Q_x = n_x\pi/x'_0$, since $Q_x D_x/\pi \approx 68 n_x$ is even. Alternatively, for n_y odd, $Q_y D_y/\pi$ is also odd, $\tau_i \neq \tau_f$ and ridges are anticipated at $Q_x = (n_x + 1/2)\pi/x'_0$, since $Q_x D_x/\pi \approx 68 n_x + 34$ is still even.

In figure 5, planes at $k = 0$, 5, and 10 show the expected rods at $Q_x = 0$ and $\pm(10.2 \pm 0.1)$ Å^{-1}. The rods at $Q_x = \pm(n_x + 1/2)\pi/x'_0$ are observed at $k = 2$ and 3, or 7 and 8. According to table 5, the intensity should be a maximum in between these planes, at $k \approx 2.6$ and 7.7, respectively. The corresponding maps (figure 6) confirm that the super-rigid reciprocal lattice is clearly distinct from the Bragg reciprocal lattice.

Note that (11) is a particular case of (12), for $Q_y = 0$. These equations were treated separately for the sake of clarity.

3.3.3. Quantum crystal. The differential cross-section for the superlattice of protons in three dimensions is

$$\frac{\mathrm{d}\sigma_3}{\mathrm{d}\Omega} = \sum_{\tau_i}\sum_{\tau_f}\left|\sum_{j=j'=1}^{N_a}\mathcal{F}_3(j) + \tau_f\tau_i \exp \mathrm{i}(Q_x D_x/2 + Q_y D_y/2)\mathcal{F}_3(j')\right|^2;$$
$$\mathcal{F}_3(j) = \sum_{k=1}^{N_b}\sum_{l=1}^{N_c} b_{\mathrm{H}jkl}\left\{\exp \mathrm{i}\left[Q_x\left(jD_x - x'_0\right) + Q_y\left(kD_y - y'_0\right) + Q_z l D_z\right]\right. \qquad (13)$$
$$\left. + \ \tau_f\tau_i \exp \mathrm{i}\left[Q_x\left(jD_x + x'_0\right) + Q_y\left(kD_y + y'_0\right) + Q_z l D_z\right]\right\}.$$

This function diverges along the rods of intensity at $Q_z = \pm n_z 2\pi/D_z$, with $n_z = 0, 1, 2, \ldots$, $D_z \approx c \times \cos 28^\circ \approx 3.28$ Å and $2\pi/D_z \approx 1.92$ Å^{-1}. The cross-section for these peaks (≈101.7 barns) is about five times that for Bragg's peaks (≈21.7 barns). The enhancement of Bragg's peaks along the ridges of intensity are clearly visible in figures 3 and 5. The rods of intensity observed at $Q_x = 0$ are essentially due to enhanced peaks, while the diffuse part cannot be distinguished from incoherent scattering. Consequently, the 'ridge' of enhanced peaks is better visible at room temperature.

In conclusion of this section, $KHCO_3$ offers the (so far unique) opportunity to observe diffraction by a super-rigid lattice: double lines [11]; grating; array; and full superlattice in three dimensions. All patterns are interpreted comprehensively with the macroscopic single particle states (6) and (7). The remarkable coincidence of the rods predicted in table 5 with observation is unlikely to be fortuitous. The sublattice of protons is entirely determined by diffraction, and there is no adjustable parameter in the calculation of the differential cross sections. (This is at variance with the model by Keen and Lovesey where S is adjustable [26].)

As long as alternative interpretations can be safely discarded, we confidently conclude that macroscopic quantum entanglement occurs in three dimensions at room temperature, on the scale of Avogadro's constant. As a matter of fact, some diffraction experiments presented above were carried out with a crystal containing $\sim 10^{22}$ protons. There is no fundamental objection to extrapolating such quantum states to bigger crystals.

4. Temperature effects: single particle macroscopic tunnelling states

Proton transfer across hydrogen bonds in centrosymmetric dimers of $KHCO_3$ is commonly represented as a thermally activated interconversion between tautomers. NMR [14, 16], quasi-elastic neutron scattering [15], and spectroscopy studies [36, 25] converge to the conclusion that proton transfer occurs via tunnelling across a quasi-symmetric double minimum potential. Two statistical mechanisms have been proposed: the pairwise synchronous transfer and the uncorrelated two-stepwise single proton transfer. However, diffraction does not confirm stochastic disordering, even at elevated temperatures (**EC2**). Consequently, statistical models based on interconversion of local dimers [37] are inappropriate.

The rods observed at 300 K indicate that the quantum coherence of the super-rigid lattice is preserved. The proton distribution at elevated temperatures must be thought of as a superposition of macroscopic states, say $|\overline{\mathbf{I}}\rangle$ and $|\overline{\mathbf{II}}\rangle$, corresponding to the different proton configurations sketched in figure 7. $|\overline{\mathbf{I}}\rangle$ is the ground state of **I**, identical to (7). Proton dynamics can be treated in exactly the same way for configuration **II** in order to construct the ground state $|\overline{\mathbf{II}}\rangle$. The two configurations are not degenerate: $|\overline{\mathbf{I}}\rangle$ is the crystal ground state, whereas $|\overline{\mathbf{II}}\rangle$ is at a higher energy and its population degree is temperature dependent. Quite remarkably, the lines of protons are identical for the two configurations. Diffraction by the superlattice is unaffected by the superposition of states and the rods of intensity are observable at any temperature.

The superposition of super-rigid states accounts for the population degrees of the proton sites as a function of the temperature but this cannot account for proton transfer dynamics. Transitions between $|\overline{\mathbf{I}}\rangle$ and $|\overline{\mathbf{II}}\rangle$ require energy transfer and, therefore, disentanglement. Then, symmetric and antisymmetric pseudoprotons become separable. Two entangled single particle states (singlet and triplet-like, respectively, each with 12-fold degeneracy) split into four disentangled states with sixfold degeneracy:

$$\begin{aligned} &|\mathbf{I}_a\rangle \otimes |\mathbf{I}_s\rangle \qquad \text{at } 0; \\ &2^{-1/2}\left[|\mathbf{II}_a\rangle \otimes |\mathbf{I}_s\rangle \pm |\mathbf{I}_a\rangle \otimes |\mathbf{II}_s\rangle\right]; \qquad \text{at } h\nu_{01}; \\ &|\mathbf{II}_a\rangle \otimes |\mathbf{II}_s\rangle; \qquad \text{at } 2h\nu_{01}. \end{aligned} \tag{14}$$

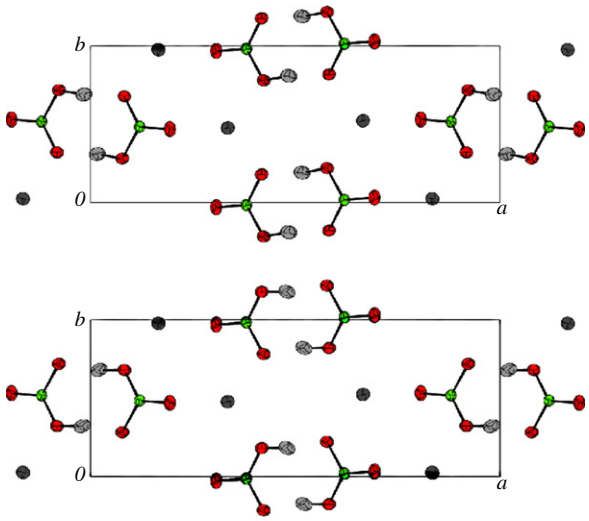

Figure 7. Schematic view of proton configurations for the entangled states $\overline{|\mathbf{I}\rangle}$ (bottom) and $\overline{|\mathbf{II}\rangle}$ (top).

The states $\overline{|\mathbf{I}\rangle}$ (entangled) and $|\mathbf{I}_a\rangle \otimes |\mathbf{I}_s\rangle$ (disentangled) on the one hand, $\overline{|\mathbf{II}\rangle}$ and $|\mathbf{II}_a\rangle \otimes |\mathbf{II}_s\rangle$ on the other, are degenerate. These disentangled states are those probed by Bragg diffraction.

In the intermediate disentangled state, a pseudoproton is transferred without destruction of the centre of symmetry (figure 8). For the sake of simplicity, we suppose the two substates are degenerate, although a splitting would not change the overall scheme. The interconversion dynamics can now be represented as a disentanglement/re-entanglement process:

$$|\mathbf{II}_a\rangle \otimes |\mathbf{I}_s\rangle \pm |\mathbf{I}_a\rangle \otimes |\mathbf{II}_s\rangle \longleftrightarrow \overline{|\mathbf{I}\rangle} \pm \overline{|\mathbf{II}\rangle}. \tag{15}$$

The energy level scheme for proton transfer dynamics is presented in figure 9. This is a two-stepwise process, each step corresponding to the transfer of a pseudoproton. In previous works, the quasi-symmetrical double minimum potential for proton transfer was determined from experimental data: the distance $2x_0'$ from the crystal structure; the potential barrier from the OH stretching bands [36]; the ground state splitting ($h\nu_{01}$) from INS [25]. This effective potential accounts for the transfer of a bare proton along a linear coordinate. This has been a puzzle, ever since it was determined, for it was difficult to rationalize the local transfer of a single proton. We now understand that this effective potential is actually a nonlocal potential for the transfer of a nonlocal pseudoproton with a mass of 1 amu. The ground state splitting can therefore be assigned to the intermediate state: $h\nu_{01} \approx 216\ \mathrm{cm}^{-1}$. (Note that there is no measurable splitting.) Then, the superposition of entangled states at thermal equilibrium

$$\overline{|\Psi(T)\rangle} = \overline{c}_{\mathbf{I}}(T)\overline{|\mathbf{I}\rangle} + \overline{c}_{\mathbf{II}}(T)\overline{|\mathbf{II}\rangle}, \tag{16}$$

with $\overline{c}^2_{\mathbf{I}}(T) + \overline{c}^2_{\mathbf{II}}(T) = 1$, gives the relative population of the secondary site as

$$\overline{c}^2_{\mathbf{II}}(T) = 2p^2_{01}(T)[1 + p^2_{01}(T)]^{-1} \tag{17}$$

where $p_{01}(T) = \exp(-h\nu_{01}/kT)$. In figure 2, the solid line is in reasonable agreement with measurements. Alternatively, the disentangled state at thermal equilibrium

$$|\Psi(T)\rangle = c_{00}(T)|\mathbf{I}_a\rangle \otimes |\mathbf{I}_s\rangle + 2^{-1/2}c_{01}(T)[|\mathbf{II}_a\rangle \otimes |\mathbf{I}_s\rangle \pm |\mathbf{I}_a\rangle \otimes |\mathbf{II}_s\rangle] + c_{11}(T)|\mathbf{II}_a\rangle \otimes |\mathbf{II}_s\rangle, \tag{18}$$

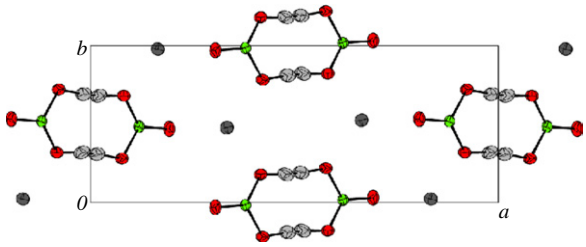

Figure 8. Schematic view of the virtual disentangled state $2^{-1/2}(|\mathbf{II}_a\rangle \otimes |\mathbf{I}_s\rangle \pm |\mathbf{I}_a\rangle \otimes |\mathbf{II}_s\rangle)$. All proton sites are equally occupied.

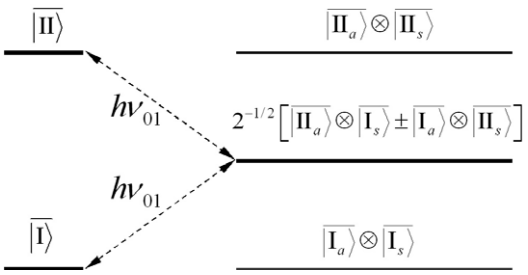

Figure 9. Energy level scheme for entangled (left) and disentangled (right) states.

with $c_{00}^2(T) + c_{01}^2(T) + c_{11}^2(T) = 1$ gives the population of the secondary site as

$$\mathcal{P}(T) = \left[p_{01}(T) + 2p_{01}^2(T)\right] P^{-1}(T), \tag{19}$$

with $P(T) = 1 + p_{01}(T) + p_{01}^2(T)$. The calculated population degree (the dashed curve in figure 2) is quite at variance with observation. Consequently, the population degree of the intermediate state is clearly negligible and does not obey Boltzmann's law. This state is virtual. It does not exist if it is not 'measured'. The potential function is also virtual. How is it related to the Born–Oppenheimer potential surface is an open question. This is a challenge for further theoretical progress. At least, semiclassical instanton methods utilized to calculate extreme tunnelling trajectories [38] can be questioned.

Figure 2 emphasizes the impact of macroscopic entanglement on the thermodynamics. It shows that entanglement can play an essential role in the evolution of a large ensemble of particles in complex systems. This result challenges the Schrödinger's cat paradox, one of the most famous paradoxes in the foundation of quantum mechanics. This paradox consists in the conclusion that a macroscopic object may be in a linear superposition of states corresponding to macroscopically different behaviours, provided that it is not observed. As opposed to this, we do observe/measure a superposition of macroscopic tunnelling states without any significant perturbation. In fact, the transition from quantum to classical is impossible for the superlattice because environment/measurement induced decoherence is automatically counterbalanced by spontaneous re-entanglement. The superposition state is therefore an objective reality, dictated by the crystal structure, regardless of whether it is observed or not. Another challenge is that any thought observation gives either a dead or an alive cat-state, with a certain probability, while experimental disentanglement of $KHCO_3$ preserves the superposition of the two proton configurations.

5. Conclusion

At any temperature up to 300 K, the sublattice of protons is a macroscopic quantum object whose dynamics is adiabatically separated from the rest of the crystal. There is no evidence for disordering and there is no transition from quantum to classical regime. Apparently, there is no upper limit on the size and complexity for time-independent entanglement at room temperature.

The cornerstones of our theoretical framework are (i) indistinguishability, (ii) adiabatic separation, (iii) the fermionic nature of protons, and (iv) degeneracy. Entanglement arises from the crystal structure and does not depend explicitly on the strength of proton–proton interactions. We define pseudoprotons ($m = 1$ amu) as nonlocal macroscopic single particle states and we show that the sublattice of protons is super-rigid and decoherence-free.

Up to room temperature, a number of protons on the scale of Avogadro's constant is in a superposition of single particle tunnelling states corresponding to distinct crystal configurations. Entanglement plays an essential role in the thermodynamics of proton transfer. On the other hand, disentanglement gives rise to virtual states that can be thought of as the transfer of a nonlocal pseudoproton across a virtual nonlocal double minimum potential.

Super-rigidity adds a crystalline solid to the list of substances with 'super' properties along with liquids (superfluidity in ^{4}He and ^{3}He), vapour (Bose–Einstein condensates of ultracold atoms) and electrons (superconductivity in metals and high-T_c copper oxides) [39].

Acknowledgment

We are indebted to N Leygue from LADIR, for preparing single crystals.

References

[1] Einstein A, Podolsky B and Rosen N 1935 Can quantum-mechanical description of physical reality be considered complete? *Phys. Rev.* **47** 777–80
[2] Bohr N 1928 The quantum postulate and recent developments of quantum theory *Nature* **121** 580
[3] Leggett A J 1980 Macroscopic quantum systems and the quantum theory of measurement *Suppl. Prog. Theor. Phys.* **69** 80–100
[4] Leggett A J and Garg A 1985 Quantum mechanics versus macroscopic realism: is the flux there when nobody looks? *Phys. Rev. Lett.* **54** 857–60
[5] Leggett A J, Chakravarty S, Dorsey A T, Fisher M P A, Garg A and Zwerger W 1987 Dynamics of the dissipative two-state system *Rev. Mod. Phys.* **59** 1–85
[6] Laloë F 2001 Quantum mechanics, strange correlations; paradoxes and theorems *Am. J. Phys.* **69** 655–701
[7] Leggett A J 2002 Testing the limits of quantum mechanics: motivation, state of play, prospects *J. Phys.: Condens. Matter* **14** R415–51
[8] Zurek W H 2003 Decoherence, einselection and the quantum origin of the classical *Rev. Mod. Phys.* **75** 715–75
[9] Chatzidimitriou-Dreismann C A, Redah T A, Streffer R M F and Mayers J 1997 Anomalous deep inelastic neutron scattering from liquid H_2O–D_2O: evidence of nuclear quantum entanglement *Phys. Rev. Lett.* **79** 2839–42
[10] Caldeira A O and Leggett A J 1983 Quantum tunnelling in a dissipative system *Ann. Phys.* **149** 374–456
[11] Ikeda S and Fillaux F 1999 Incoherent-elastic-neutron scattering study of the vibrational dynamics and spin-related symmetry of protons in the $KHCO_3$ crystal *Phys. Rev.* B **59** 4134–45
[12] Fillaux F, Cousson A and Keen D 2003 Observation of the dynamical strucuture arising from spatially extended quantum entanglement and long-lived quantum coherence in the $KHCO_3$ crystal *Phys. Rev.* B **67** 054301
Fillaux F, Cousson A and Keen D 2003 *Phys. Rev.* B **67** 189901 (erratum)
[13] Fillaux F 1998 The pauli principle and the vibrational dynamics of protons in solids: a new spin-related symmetry *Physica* D **113** 172–83
[14] Benz S, Haeberlen U and Tegenfeldt J 1986 Jump motion of deuterons along hydrogen bonds in $KDCO_3$. A deuteron relaxation study *J. Magn. Reson.* **66** 125–34

[15] Eckold G, Grimm H and Stein-Arsic M 1992 Proton disorder and phase transition in $KHCO_3$ *Physica* B **180/181** 336–8
[16] Odin C 2004 ^{13}C and ^{39}K high-resolution solid-state NMR study of the nonferroic phase transition of potassium hydrogen carbonate. Complementarity between NMR and incoherent neutron scattering *J. Phys. Chem.* B **108** 7402–11
[17] http://www-llb.cea.fr
[18] Thomas J O, Tellegren R and Olovsson I 1974 Hydrogen-bond studies. LXXXIV. An x-ray diffraction study of the structures of $KHCO_3$ and $KDCO_3$ at 298, 219 and 95 K *Acta Crystallogr.* B **30** 1155–66
[19] Thomas J O, Tellegren R and Olovsson I 1974 Hydrogen bond studies. XCII. Disorder in $(HCO_3)_2^{2-}$ and $(DCO_3)_2^{2-}$ dimers: A neutron diffraction study of $KHCO_3$ and $KDCO_3$ *Acta Crystallogr.* B **30** 2540–9
[20] Nield V M and Keen D A 2001 *Diffuse Neutron Scattering from Crystalline Materials* (*Oxford Series on Neutron Scattering in Condensed Matter* vol 14) (Oxford: Clarendon)
[21] Haussühl S 1986 Anomalous elastic behaviour of moniclinic potassium hydrogen carbonate, $KHCO_3$, in the vicinity of the phase transition at 318 k *Solid State Commun.* **57** 643–7
[22] Kashida S and Yamamoto K 1990 Structural transition in $KHCO_3$ *J. Solid State Chem.* **86** 180–7
[23] http://www.isis.rl.ac.uk/crystallography
[24] Ikeda S, Kashida S, Sugimoto H, Yamada Y, Bennington S M and Fillaux F 2002 Inelastic neutron scattering study of the localized dynamics of protons in $KHCO_3$ single crystals *Phys. Rev.* B **66** 184302
[25] Fillaux F, Tomkinson J and Penfold J 1988 Proton dynamics in the hydrogen bond. The inelastic neutron scattering spectrum of potassium hydrogen carbonate at 5 K *Chem. Phys.* **124** 425–37
[26] Keen D A and Lovesey S W 2003 Quantum correlation between protons in potassium bicarbonate *J. Phys.: Condens. Matter* **15** 4937–46
[27] Fillaux F and Cousson A 2004 Comment on 'quantum correlations between protons in potassium bicarbonate' *J. Phys.: Condens. Matter* **16** 1007–10
[28] Keen D A and Lovesey S W 2004 Reply to comment on 'quantum correlations between protons in potassium bicarbonate' *J. Phys.: Condens. Matter* **16** 5637–8
[29] Lovesey S W 2005 Quantum mechanical correlations between spatial and spin degrees of freedom in a material as revealed by neutron scattering *Phys. Scr.* **71** cc14
[30] Sugimoto H, Okumura A and Yuuki H 2006 Effects of entanglement on elastic and inelastic scattering functions for neutron scattering from a pair of nuclei in solids *Phys. Rev.* B **73** 014305
[31] Schuster P, Zundel G and Sandorfy C 1976 *The Hydrogen Bond. Recent Developments in Theory and Experiments* vol I, II and III (Amsterdam: North-Holland)
[32] Cowley R A 2003 Quantum entanglement and neutron scattering experiments *J. Phys.: Condens. Matter* **15** 4143–52
[33] Novack A 1974 Hydrogen bonding in solids. Correlation of spectroscopic and crystallographic data *Struct. Bond.* **18** 177–216
[34] Cohen-Tannoudji C, Diu B and Laloë F 1977 *Mécanique Quantique* (Paris: Hermann)
[35] Lovesey S W 1984 *Nuclear Scattering, Theory of Neutron Scattered from Condensed Matter* vol I (Oxford: Clarendon)
[36] Fillaux F 1983 Calculation of infrared and raman band profiles of strong hydrogen bonds. OH stretching band and proton dynamics in crystalline potassium hydrogen carbonate *Chem. Phys.* **74** 405–12
[37] Skinner J L and Trommsdorff H P 1988 Proton transfer in benzoic acid crystals: a chemical spin-boson problem. Theoretical analysis of nuclear magnetic resonance, neutron scattering, and optical experiments *J. Chem. Phys.* **89** 897–907
[38] Smedarchina Z, Fernandez-Ramos A and Siebrand W 2005 Tunneling dynamics of double proton transfer in formic acid and benzoic acid dimers *J. Chem. Phys.* **122** 134309
[39] Babaev E, Sudbø A and Ashcroft N W 2005 Observability of a projected new state of matter: a metallic superfluid *Phys. Rev. Lett.* **95** 105301